Supplementary Information

Strong hydrogen trapping by tangled dislocations in cold-drawn pearlitic steels

Chao Huang[1,2,+], Chuanjie Cui[3,+], Ranming Niu[1,2,+,*], Fenghua Lu[4], Cheng-Yun Wu[1,5], Xiaoxiong Zhu[6], Hongzhou Lu[7], Yongqing Zhang[7], Pang-Yu Liu[1,2], Bosheng Dong[1,2], Yi-Hsuan Sun[1,8], Hongjian Wang[2], Wei Li[4], Hung-Wei Yen[8,9], Aimin Guo[7], Julie M. Cairney[1,2,*], Emilio Martínez-Pañeda[3,*], Eason Yi-Sheng Chen[1,10,*]

[1] Australian Centre for Microscopy and Microanalysis, The University of Sydney, Sydney, NSW, 2006, Australia

[2] School of Aerospace, Mechanical and Mechatronic Engineering, The University of Sydney, Sydney, NSW, 2006, Australia

[3] Department of Engineering Science, The University of Oxford, Oxford, OX1 3PJ, United Kingdom

[4] School of Materials Science and Engineering, Shanghai Jiao Tong University, Shanghai, 200240, China

[5] School of Biomedical Engineering, The University of Sydney, Sydney, NSW, 2006, Australia

[6] Jiangsu Tokyo Rope Co., Ltd., Jiangyin, Jiangsu, 214445, China

[7] CITIC Metal Co., Beijing, 100004, China

[8] Department of Materials Science and Engineering, National Taiwan University, Taipei, 10617, Taiwan

[9] Advanced Research Center for Green Materials Science and Technology, National Taiwan University, Taipei, 10617, Taiwan

[10] School of Materials Science and Engineering, Nanyang Technological University, Singapore, 639798, Singapore

[+] The authors contributed equally to this work.
*Corresponding authors: eason.chen@ntu.edu.sg (E. Y.-S. C.); emilio.martinez-paneda@eng.ox.ac.uk (E. M.-P.); ranming.niu@sydney.edu.au (R. N.); julie.cairney@sydey.edu.au (J. M. C.)

This document contains the following content:

- Figs. S1 to S10
- Tables S1 to S3
- Captions of Movies S1 and S2

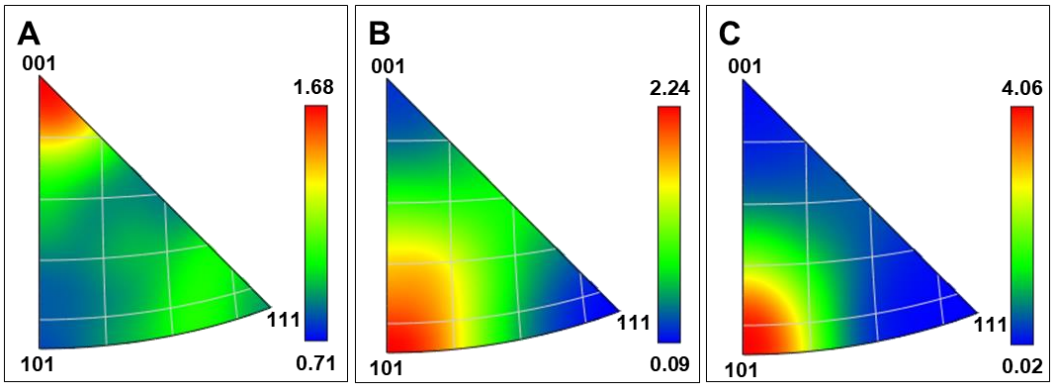

Fig. S1 EBSD pole figures. *(A) unstrained, (B) mid-strained and (C) high-strained samples.*

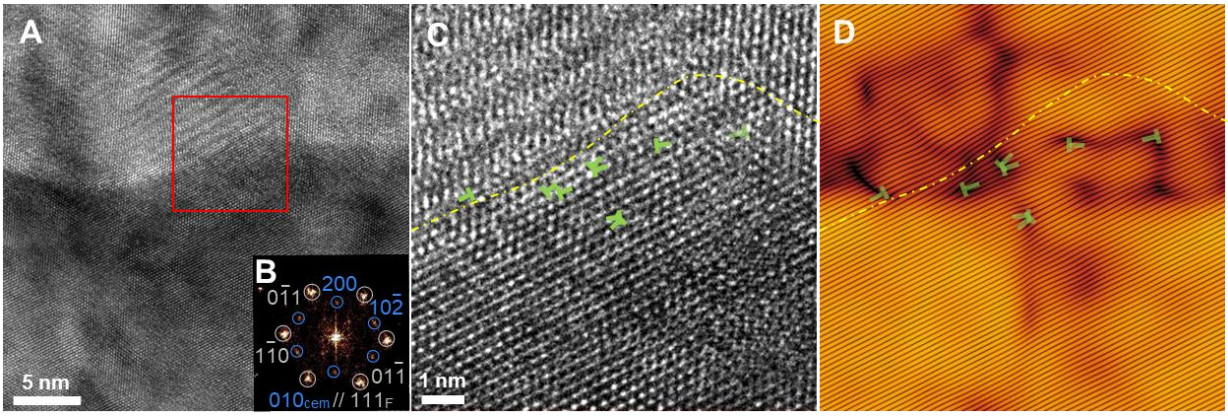

Fig. S2 HRTEM analysis of a ferrite/cementite interface and interfacial dislocations in the specimens at a cold-drawn rate of 1.67. *(**A**) HRTEM image of an interface between cementite and ferrite, showing the step-shape at the interface. (**B**) The fast Fourier transform (FFT) pattern of (A), demonstrates the orientation relationship between ferrite (111) and cementite (010). (**C**) A zoon-in image of a red square in the (A) showing the step-shape area (yellow dash line) bulges from the interface and a high density of misfit dislocations marked by green symbols. (**D**) The inverse FFT (iFFT) graph derived from (C). These graphs proved that a high density of misfit dislocations was storage at the ferrite/cementite interface as interfacial dislocations, causing the step-shaped area.*

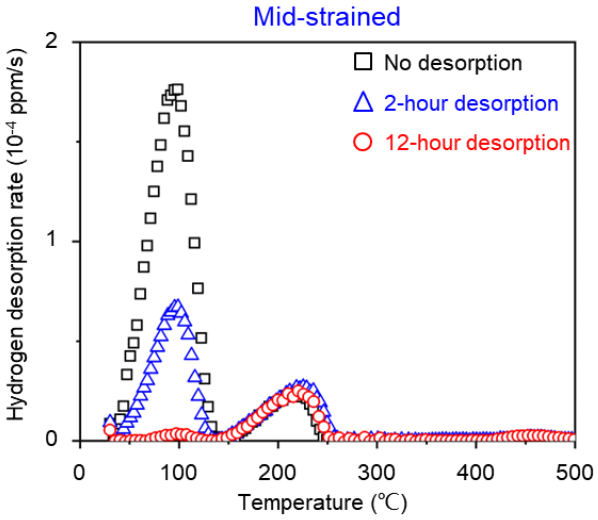

Fig. S3 TDS results of mid-strained specimens. *H-charged (red), H-charged and desorbed for 2 hours (blue), and H-charged and desorbed for 12 hours (red).*

Table S1 TDS measured hydrogen contents.

Specimen	Hydrogen desorption condition	Low-temperature peak H content (mass ppb)	High-temperature peak H content (mass ppb)	Total H content (mass ppb)
Unstrained	No desorption	643	Not detectable	643
	2 hours	137	Not detectable	137
	12 hours	Not detectable	Not detectable	Not detectable
Mid-strained	No desorption	2162	238	2400
	2 hours	519	264	783
	12 hours	20	248	268
High-strained	No desorption	3280	614	3894
	2 hours	1103	467	1570
	12 hours	34	500	534

Table S2 SSRT results

Sample	Condition	Sample number	Ultimate tensile testing (GPa)	Ductility (%)	Ductility loss (%)	Error (%)
Unstrained	Uncharged	1	1.364	10.2	-	-
		2	1.300	10.5		
		3	1.343	9.4		
	H-charged	1	1.247	8.1	22.1	3.4
		2	1.340	7.4		
		3	1.280	7.9		
	H-desorbed	1	1.360	9.5	1.7	7.6
		2	1.279	9.4		
		3	1.354	10.8		
High-strained	Uncharged	1	2.202	6.5	-	-
		2	2.180	6.5		

		3	2.125	5.6		
	H-charged	1	2.120	5.2	14.4	3.9
		2	2.087	5.6		
		3	2.020	5.1		
	H-desorbed	1	2.105	5.7	3.0	8.8
		2	2.127	6.5		
		3	2.220	5.5		

SEM fracture surface observation

Scanning electron microscopy (SEM) observations were conducted using a Zeiss ULTRA Plus microscope, operated at an acceleration voltage of 10 kV. The fracture surface analyses of both unstrained and heavily strained specimens under different conditions—uncharged, hydrogen-charged, and hydrogen-charged followed by desorption—are described as follows.

Fig. S4A shows the fracture surface of an unstrained specimen, revealing numerous dimples (highlighted by red arrows), which are characteristic of ductile fracture. In contrast, Fig. S6B illustrates the fracture surface of an unstrained specimen after hydrogen charging, where a reduced area of dimples is visible, along with numerous cleavage planes (emphasized by blue arrows), indicating a loss of ductility. Fig. S4D presents the fracture surface of a heavily strained specimen, displaying a mix of fine dimples, cleavage planes, and brittle secondary cracks (marked by green arrows), resulting in a mixed fracture pattern combining both brittle and ductile characteristics. This mixed fracture contributes to the specimen's retained ductility. However, after hydrogen charging, the heavily strained specimen shows very few dimpled regions, an increased presence of cleavage planes, and extensive, elongated cracks, leading to severe embrittlement, as shown in Fig. S4E. The fracture surfaces of hydrogen-charged and desorbed specimens exhibit similar features to the uncharged specimens, as illustrated in Figs. S4C and S4F.

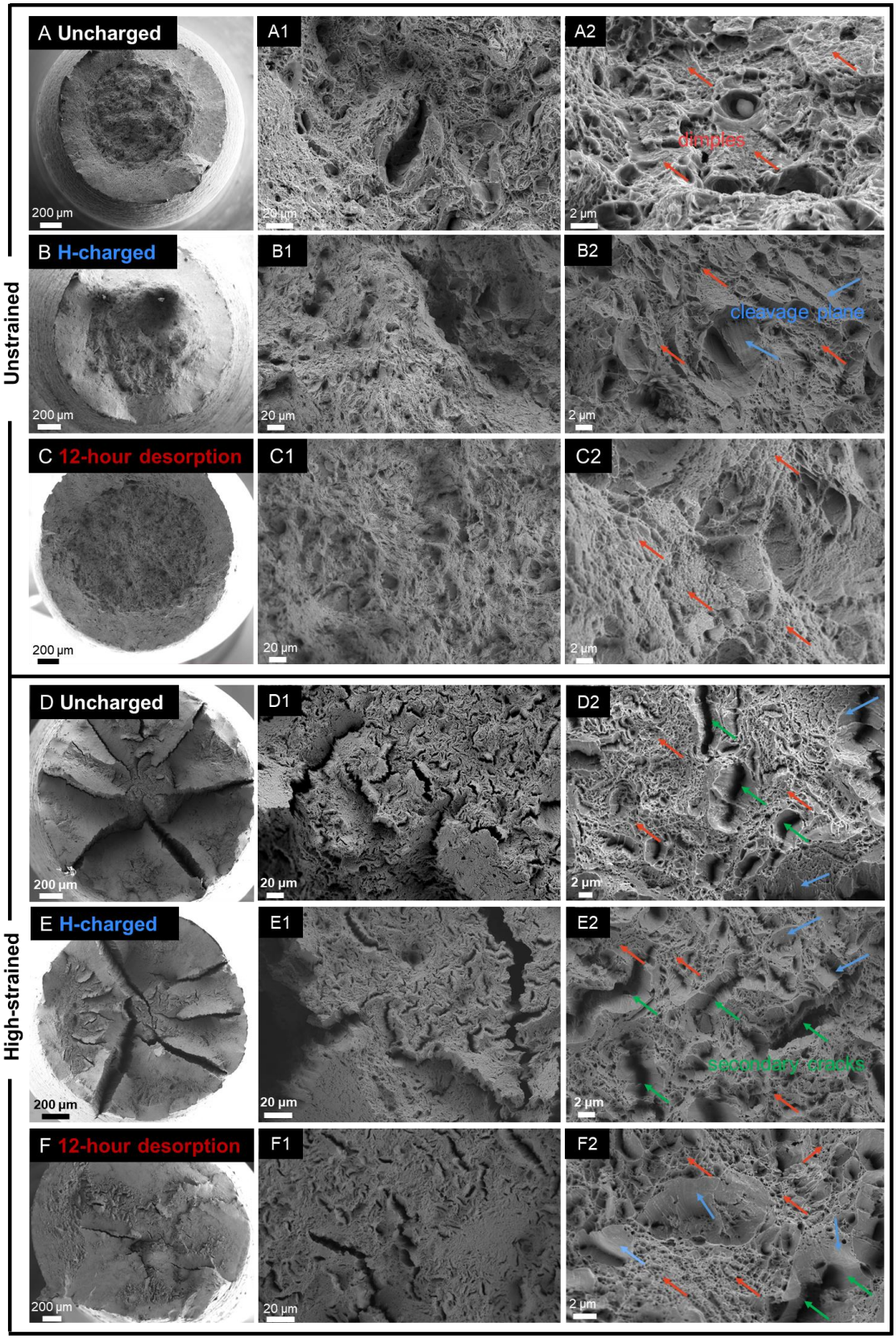

Fig. S4 SEM fracture surface observation. *Figure A-C are unstrained specimens. Figure D-F are high-strained specimens. Each includes H-charged (white), H-charged and desorbed for 2 hours (blue), and H-charged and desorbed for 12 hours (red).*

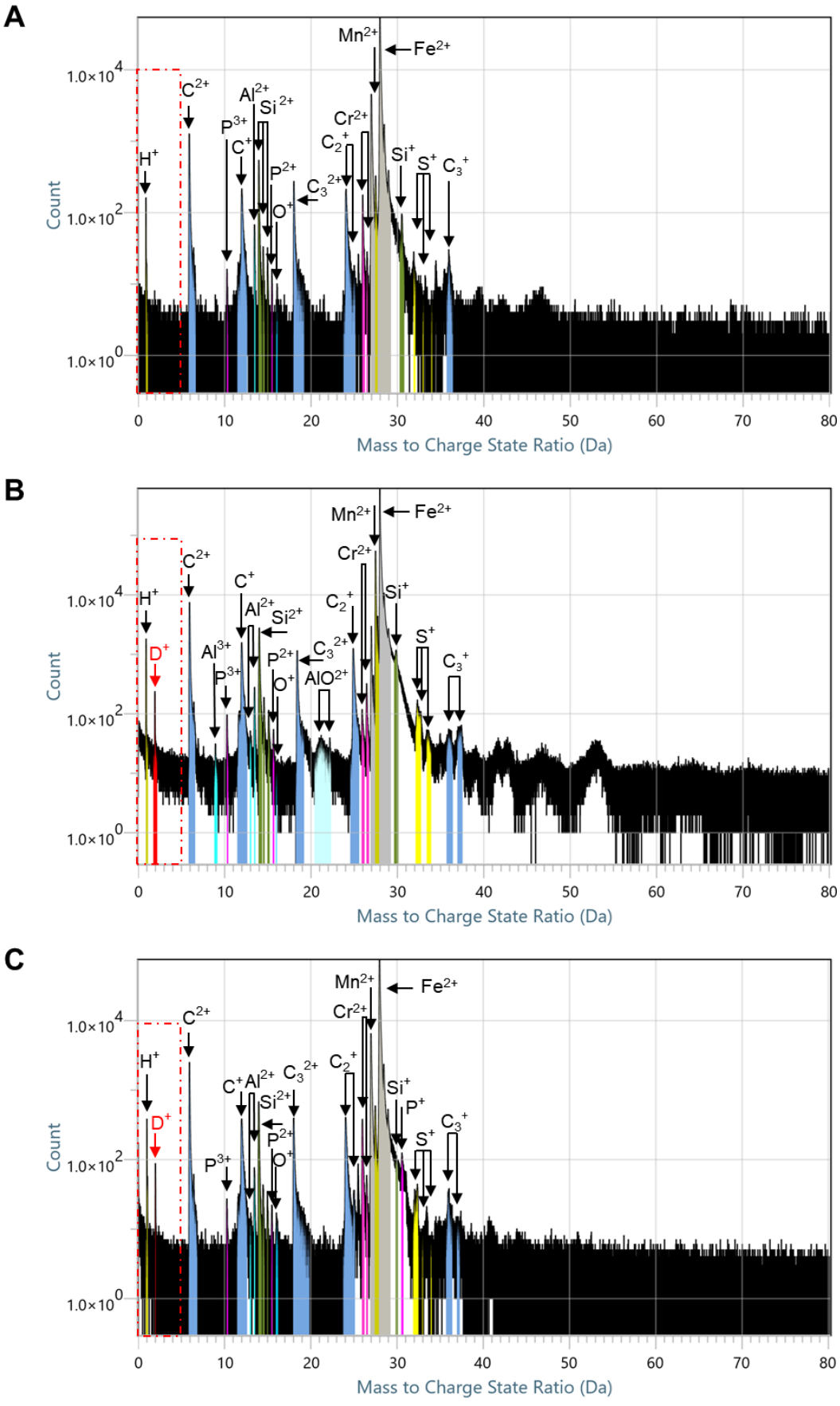

Fig. S5 APT mass spectra of high-strained specimens. *(A) uncharged,* ***(B)***

*deuterium-charged and cryo-transfer, (**C**) deuterium-charged and then desorbed for 2 hours.*

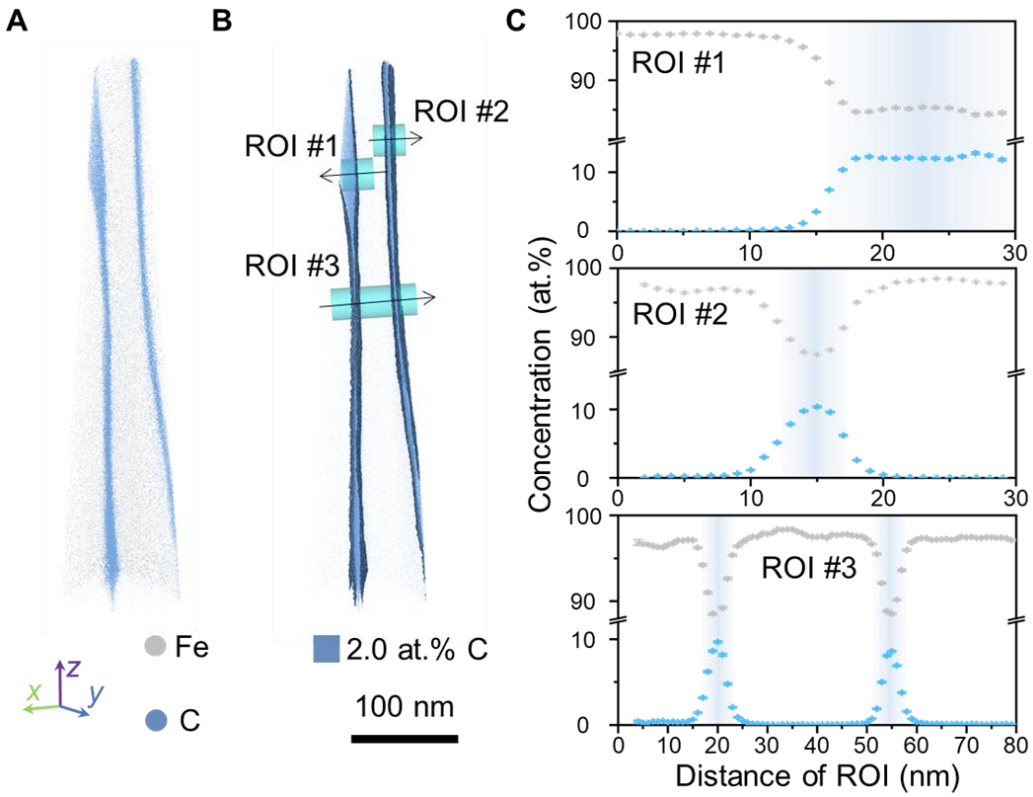

Fig.S6 Additional 3D APT analysis of an uncharged strained sample. (A) *Reconstructed atom map showing Fe atoms in grey and C atoms in blue.* ***(B)*** *Isoconcentration surfaces at 2.0 at. % C highlighting cementite regions.* ***(C)*** *Carbon and Fe concentration profiles across three regions of interest (ROI #1–3), each traversing ferrite and cementite. The blue shaded area represents the cementite region. In the relatively wider cementite region (ROI #1), the maximum carbon concentration reaches 13.2 at. %, whereas a neighboring cementite lamella exhibits only 10.3 at. % in ROI #2. In ROI #3, which intersects two adjacent cementite lamellae, the maximum concentrations are 9.6 at. % and 8.5 at. %, respectively. These observations show that within a single sample, cementite compositions can vary potentially due to inhomogeneous decomposition.*

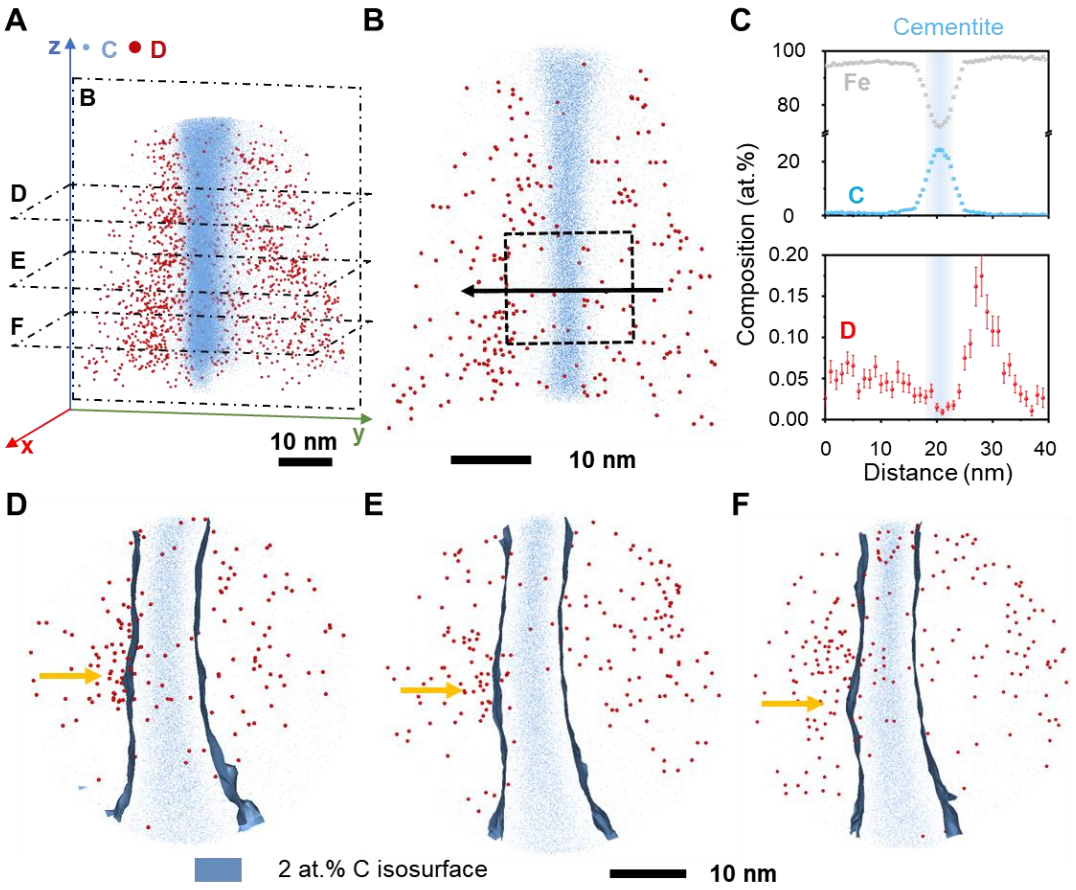

Fig. S7 *Additional APT result for 2-hour hydrogen-desorbed strained steel specimen.* ***(A)*** *is a reconstructed 3-dimensional atom map, where carbon (C) and deuterium (D) atoms are shown in blue and in red, respectively.* ***(B)*** *is a 10-nm-thick slice view of the region in the y-z plane marked by the black dashed lines in (A).* ***(C)*** *provides the elemental concentrations of iron (grey), carbon (blue), and deuterium (red) from the 30 nm x 40 nm cylindric region of interest marked by the black dashed lines in (B).* ***(D–F)*** *are 5-nm-thick slices from the x-y planes marked by the dashed lines in (A), using 2 atomic percent carbon isosurfaces to highlight the carbon-rich regions.*

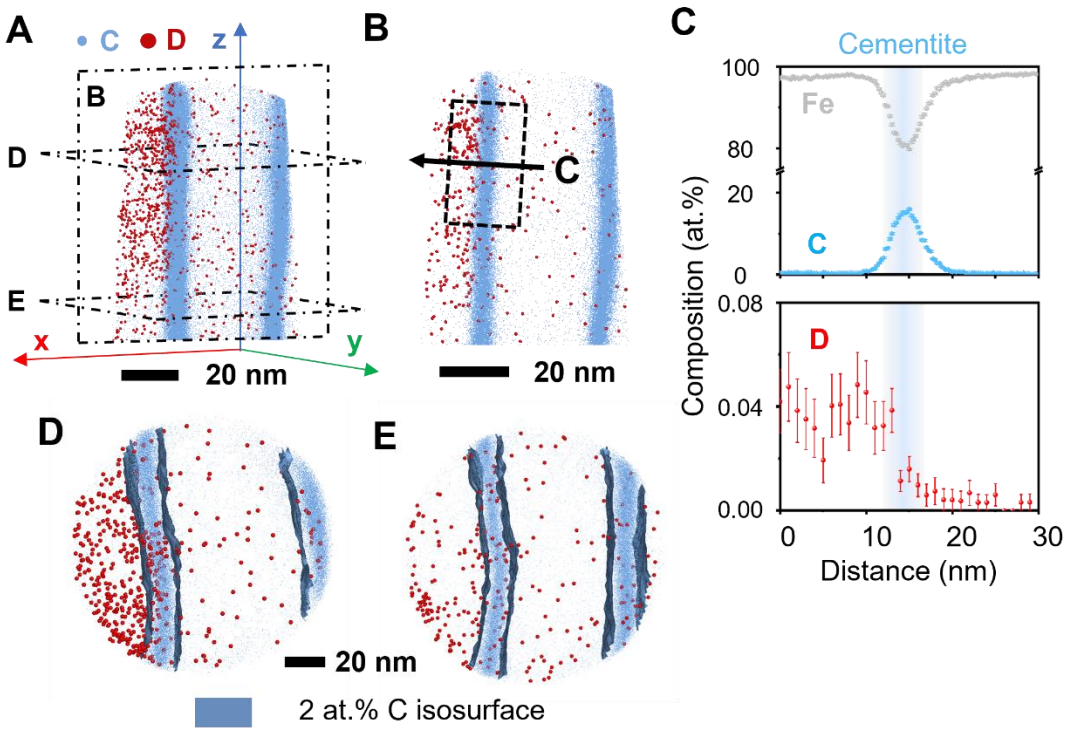

***Fig. S8** Additional APT result for 1-hour hydrogen-desorbed strained steel specimen. (A) is a reconstructed 3-dimensional atom map, where carbon (C) and deuterium (D) atoms are shown in blue and in red, respectively. (**B**) is a 10-nm-thick slice view of the region in the y-z plane marked by the black dashed lines in (A). (**C**) provides the elemental concentrations of iron (grey), carbon (blue), and deuterium (red) from the 30 nm x 30 nm cylindric region of interest marked by the black dashed lines in (B). (**D**–**E**) are 5-nm-thick slices from the x-y planes marked by the dashed lines in (A), using 2 atomic percent carbon isosurfaces to highlight the carbon-rich regions.*

***Table S3** Parameters used for the simulated hydrogen desorption profile in Fig. 7A.*

Parameters	Values	References
Diffusion coefficient D_0	1.4×10^{-8} m^2/s	(6)
Activation energy E_t	9.31 kJ/mol	(6)
Number of interstitial sites N_L	5.1×10^{29}/m^3	(7)
Activation energy for weak traps E_{wk}	30.2 kJ/mol	*TDS (Fig. 2D)*
Trapping density of weak traps N_{wk}	7.0×10^{27}/m^3	*Fitted*
Activation energy for strong traps E_{st}	80 kJ/mol	*Fitted*
Trapping density of strong traps N_{st}	1.3×10^{24}/m^3	*Fitted*
Initial lattice hydrogen C_{L0}	0.21 mol/m^3	*Fitted*
Heating rate ϕ	0.028 K/s (100 °C/hour)	*TDS (Fig. 2C)*

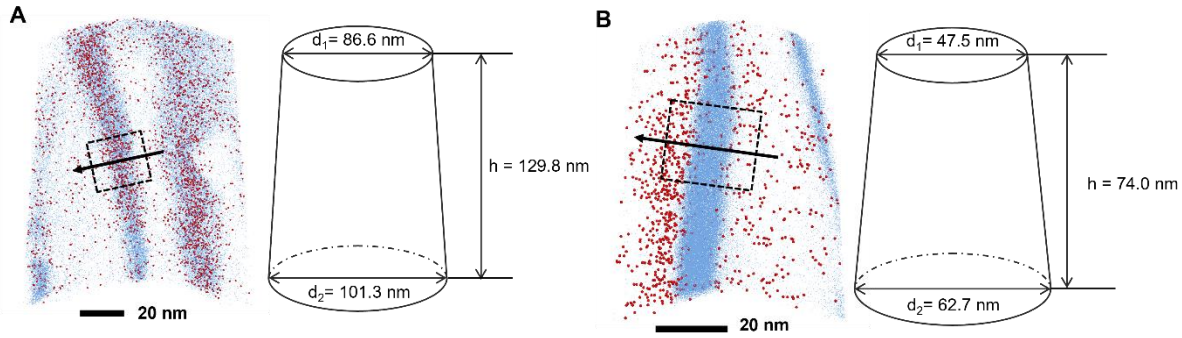

Fig. S9 *APT specimen size used in numerical simulations.*

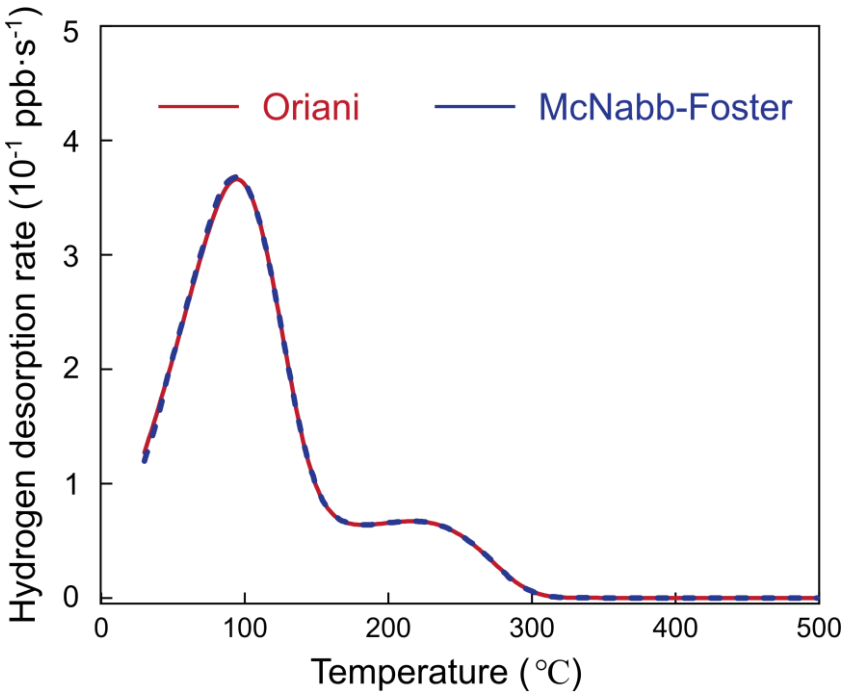

Fig. S10 *Comparison of TDS predictive results using Oriani's local equilibrium theory and the McNabb-Foster equations with a Debye frequency.*

Caption of Movies S1: 3-dimensional APT reconstruction of cryo-transfer high-strained steel specimen

Caption of Movies S2: 3-dimensional APT reconstruction of hydrogen-desorbed high-strained steel specimen.